

## RESEARCH ARTICLE

10.1002/2016JC012308

## GNSS-R nonlocal sea state dependencies: Model and empirical verification

David D. Chen-Zhang<sup>1</sup>, Christopher S. Ruf<sup>2</sup>, Fabrice Ardhuin<sup>3</sup>, and Jeonghwan Park<sup>4</sup>

## Key Points:

- Ocean wind radars sense nonwind sea state dependencies
- Long-wave (swell) effects on radar measurements are modeled
- New model predictions agree better with observations than previous models

## Correspondence to:

C.S. Ruf,  
cruf@umich.edu

## Citation:

Chen-Zhang, D. D., C. S. Ruf, F. Ardhuin, and J. Park (2016), GNSS-R nonlocal sea state dependencies: Model and empirical verification, *J. Geophys. Res. Oceans*, 121, 8379–8394, doi:10.1002/2016JC012308.

Received 2 SEP 2016

Accepted 7 NOV 2016

Accepted article online 11 NOV 2016

Published online 30 NOV 2016

<sup>1</sup>Electrical and Computer Engineering Department, University of Michigan, Ann Arbor, Michigan, USA, <sup>2</sup>Climate and Space Department, University of Michigan, Ann Arbor, Michigan, USA, <sup>3</sup>Laboratory of Ocean Physics and Satellite Oceanography, University of Brest, CNRS, Ifremer, IRD, Plouzane, France, <sup>4</sup>ElectroSciences Laboratory, The Ohio State University, Columbus, Ohio, USA

**Abstract** Global Navigation Satellite System Reflectometry (GNSS-R) is an active, bistatic remote sensing technique operating at L-band frequencies. GNSS-R signals scattered from a rough ocean surface are known to interact with longer surface waves than traditional scatterometry and altimetry signals. A revised forward model for GNSS-R measurements is presented which assumes an ocean surface wave spectrum that is forced by other sources than just the local near-surface winds. The model is motivated by recent spaceborne GNSS-R observations that indicate a strong scattering dependence on significant wave height, even after controlling for local wind speed. This behavior is not well represented by the most commonly used GNSS-R scattering model, which features a one-to-one relationship between wind speed and the mean-square-slope of the ocean surface. The revised forward model incorporates a third generation wave model that is skillful at representing long waves, an anchored spectral tail model, and a GNSS-R electromagnetic scattering model. In comparisons with the spaceborne measurements, the new model is much better able to reproduce the empirical behavior.

## 1. Introduction and Overview

Global Navigation Satellite System Reflectometry (GNSS-R) is a relatively young remote sensing technique proposed to measure geophysical quantities such as ocean surface roughness and wind speed. With it quickly gaining momentum [Zavorotny *et al.*, 2014], there has been rapid and ongoing development of instrumentation [e.g., Gleason *et al.*, 2016], retrieval algorithms [e.g., Clarizia *et al.*, 2014], and scattering models [e.g., Zavorotny and Voronovich, 2000; Lin *et al.*, 1999]. GNSS-R is a relatively low-cost technique which leverages existing navigation signals as the transmitter half of the bistatic radar system. This technique makes use of a forward scattering geometry, in contrast to conventional monostatic scatterometers and altimeters, which use a back scattering geometry. The frequency of operation is dictated by the transmitters, which are typically L-band (1–2 GHz) navigation satellites.

The combination of L-band signals and forward scattering geometry has been rarely used in the past by remote sensing instruments, and thus brings about new implications for electromagnetic interaction with surface features. In particular, bistatic L-band radar return is dominated by quasi-specular scattering, which is dictated by waves longer than about 3 times the electromagnetic wavelength [e.g., Valenzuela, 1978; Brown, 1978]. In the ocean, L-band GNSS-R is therefore sensitive to surface waves of about 50 cm in wavelength and longer. In contrast, for radar scatterometers, according to two-scale models, these 50 cm waves are tilting waves that bring about mostly secondary effects compared to the primary Bragg scatterers. Although radar altimeter scattering is also primarily quasi-specular, they typically operate at higher C-band (5 GHz) or Ku-band (13 GHz) frequencies (e.g., TOPEX/Poseidon ALT) [Fu *et al.*, 1994], which correspond to wavelengths of order one centimeter. For typical ocean roughness spectra, these centimeter scale features dominate the roughness, so the ~50 cm scale waves in most cases play only a minor role for altimetric sensors.

Modeling GNSS-R ocean scattering at L-band presents novel challenges. Short gravity waves tens of centimeters long are in a different regime than the millimeter capillary waves, because they are governed by different physics. With surface tension being negligible, these short gravity waves take longer to dissipate and propagate further before decaying. There have been questions [Cardellach *et al.*, 2014] and results showing

nonnegligible GNSS-R sensitivity to long gravity waves. However, such waves have yet to be taken into account in GNSS-R forward models. For example, the end-to-end simulator for the upcoming Cyclone Global Navigation Satellite System (CYGNSS) mission [C. S. Ruf *et al.*, 2016] uses the Katzberg relationship to model the roughness, which assumes that the scattering cross section is determined by the local, instantaneous wind speed alone [C. Ruf *et al.*, 2016]. The limitation of this assumption is illustrated in section 3, below, in which spaceborne scattering measurements are shown to exhibit large differences from those predicted by the Katzberg-model (e.g., Figures 8 and 9). The differences are most pronounced, and considered significant, at lower wind speeds.

In this paper, our objective is to develop, and then experimentally validate, a more accurate GNSS-R forward model by incorporating forcing effects other than local winds. In section 2, we present the model, which includes a third-generation wave model that has not previously been incorporated into a GNSS-R forward model. The rationale for the choice of the surface model and parameters therein are discussed. In section 3, we compare spaceborne measurements with our model predictions and with the predictions produced by the Katzberg model. We conclude with a discussion of some of the nonlocal effects that contribute to the scattering measurements predicted by our model, and consider other, second-order, effects that have not been incorporated into the model but could be as future work.

## 2. The Forward Model

### 2.1. Surface Wave Models

For phase-averaging surface wave models, one important goal is to quantify the spectral energy accurately in the form of a wave spectrum, which can range from a one-dimensional directionally integrated spectrum in the simplest case to a full three-dimensional frequency-wavenumber-direction spectrum for linear and nonlinear waves. These models can generally be divided into two types: (1) empirical models based on dimensional analysis and parameterized by wind speed and, possibly, wave age, and (2) spectral evolution models based on the energy-balance equation.

The first type constrains the shape of the spectrum, which is typically a smooth function of the input parameters. Usually, conditions are classified as duration or fetch-limited [Hwang and Wang, 2004], and the wave age is computed accordingly. The wave age and wind speed are then used to parameterize the wave spectrum. The Pierson-Muskowitz [Pierson and Moskowitz, 1964], JONSWAP [Hasselmann *et al.*, 1973], Elfouhaily [Elfouhaily *et al.*, 1997], and Hwang [Hwang *et al.*, 2013] spectra are of this type. The second type of model includes WAVEWATCH3 [Tolman and the WAVEWATCH III Development Group, 2014] (denoted by WW3 hereafter), University of Miami Wave Model [Donelan *et al.*, 2012], SWAN [Booij *et al.*, 1999], and WAM [Komen *et al.*, 1994]. These models solve the energy balance equation numerically, a Eulerian form of which in simple cases (conditions given below) may be expressed as

$$\frac{\partial E(k, x, t)}{\partial t} + c_g \frac{\partial E(k, x, t)}{\partial x} = S(k, x, t), \quad (1)$$

where  $E$  is the one-dimensional wavenumber-direction spectrum with SI units of  $\text{m}^3$ , with the wavenumber energy spectrum being  $\rho g E$  with units of  $\text{J/m}$ .  $\rho$  is the mass density of sea water, and  $g$  is the gravitational constant.  $c_g$  is the group velocity in the  $x$  direction.  $S(k, x, t)$  is the collective source term combining the effects of wind input, whitecapping dissipation, and nonlinear wave-wave interaction. Equation (1) models the temporal evolution and spatial propagation of the elevation variance of a one-dimensional wave in deep water and neglects the effects of currents. In practice, an equation of this type is discretized and integrated in time and space to solve for the wave spectrum at each time step and grid point. The source terms, with improved understanding of wave physics, have undergone significant development in the last 50 years, and are now in their "3<sup>rd</sup> generation" [Komen *et al.*, 1994].

For the second type of wave model, rather than having an a priori form, the individual source terms are crafted, and the spectrum is left free to evolve. Before the 1950s, models of the first kind were used for wave forecasting. However, several aspects are challenging for the parametric models to handle, such as the accounting for swell generated afar, and irregular bathymetry and coastlines [Ardhuin, 2016, p.52]. In addition, Chen *et al.* [2016] found that two such empirical models show significant errors in modeling the response time of waves to wind in general conditions, while later investigations showed the third-generation model WW3 performs significantly better in comparisons with in situ measurements.

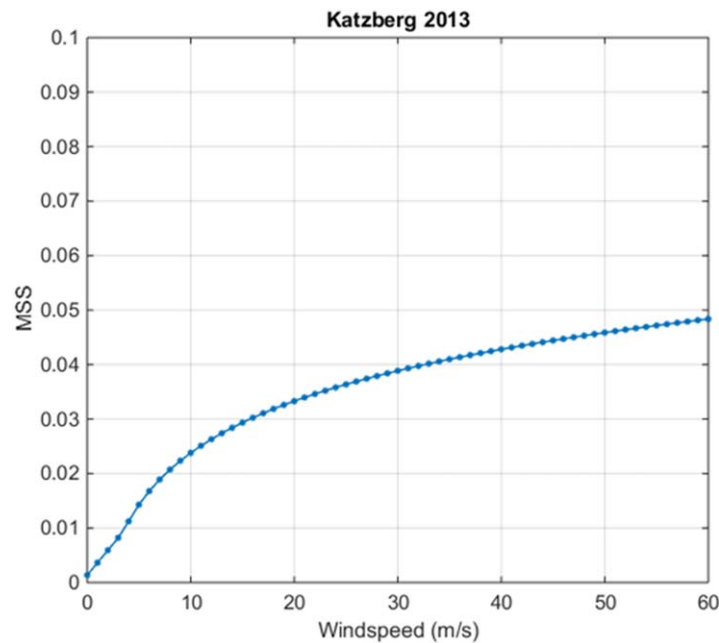


Figure 1. The Katzberg U10-mss relationship.

Despite its shortcomings, the parametric models and the associated experiments that led to them, are widely used when modeling idealized duration and fetched-limited cases. These ideal cases have been invaluable in the development of the spectral-evolution models' source terms, and they continue to serve as reference calibration points for the state-of-the-art third generation models. Moreover, these parametric models are considered the current state-of-the-art models for high-frequency waves. The form and shape of the spectral tail assumed in the model is still an area of active research [Ex. Plant, 2015, Reichl et al., 2014; Hwang et al., 2013], partly due to the challenges in their accurate measurement [Hwang, 2005].

Many electromagnetic models to-date have incorporated these parametric models [e.g., Voronovich and Zavorotny, 2001; Apel, 1994; Hwang and Fois, 2015] as the surface wave model, with the inverse wave age often set to 0.84 for "well-developed" conditions. It should be noted that formulations of source term balance of short Bragg waves have been attempted [e.g. Lyzenga and Bennett, 1988], but much uncertainty remain [Hwang et al., 2013].

For GNSS-R, the surface roughness of relevance is the low-pass-filtered mean square slope (mss)

$$LP_{mss}(k_u) = \int_0^{k_u} k^2 S(k) dk \tag{2}$$

Empirically, Brown [1978] found  $k_u = \frac{2\pi \cos \theta}{3\lambda}$  to be a suitable cutoff, with  $\lambda$  being the electromagnetic wavelength and  $\theta$  denoting the incidence angle of the observation. For the GPS L1 carrier with a frequency of 1.575 GHz, and typical incidence angles of less than 35°,  $k_u \approx 10$  rad/m, so waves of about 60 cm and longer are sensed by GNSS-R. We mention in passing that the quantity significant wave height, usually denoted as  $H_s$  and used in our analysis in section 3, can be computed from the wavenumber spectrum as

$$H_s = 4 \sqrt{\int_0^{\infty} S(k) dk} \tag{3}$$

Once the wave spectrum is known,  $LP_{mss}$  can be readily calculated. Katzberg et al. [2013] developed a semi-empirical, one-to-one relationship between wind speed and mean squared slope by fitting data provided by airborne GNSS-R experiments and an adjusted high-resolution wind speed model. The Katzberg model is even simpler than the parametric wave models because it does not involve the wave spectrum. This relationship is expressed as follows

$$\begin{aligned} LP_{mss} &= 0.45(0.00316f(U_{10}) + 0.00192f(U_{10}) + 0.003) \\ f(U_{10}) &= U_{10}, & 0 < U_{10} < 3.49 \text{ m/s} \\ f(U_{10}) &= 6 \ln(U_{10}) - 4, & 3.49 < U_{10} < 46 \\ f(U_{10}) &= 0.411U_{10}, & 46 < U_{10} \end{aligned} \tag{4}$$

where  $U_{10}$  is the wind speed at 10 m height. It is plotted in Figure 1.

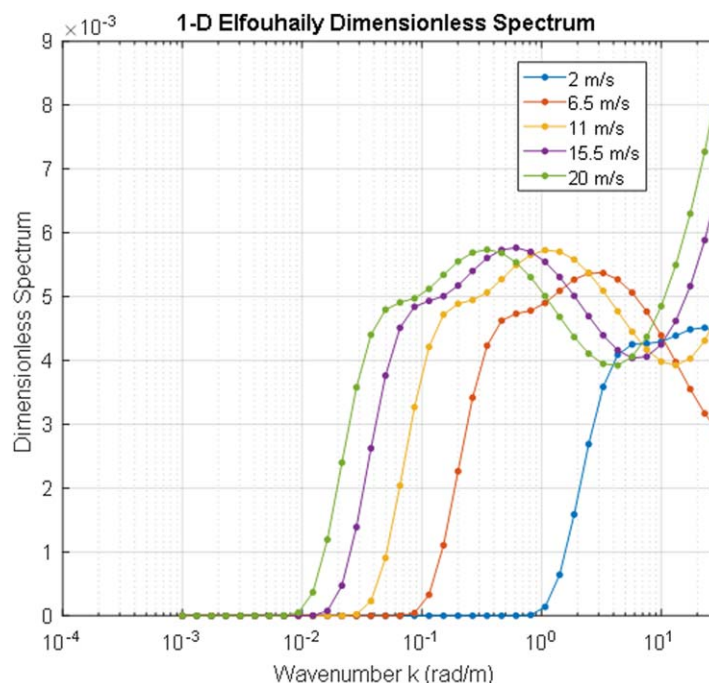


**Figure 2.** Elfouhaily slope spectrum in area-conservative form. The relevant portion for GNSS-R is about 10 rad/m and below.

peak (such as  $H_s$  and  $T_p$ ) [e.g., *The WAMDI Group*, 1988; *Ardhuin et al.* 2010; *Chu et al.*, 2004], we make use of this type of model in our work. In particular, we select WAVEWATCH III<sup>®</sup> (WW3) as the low-frequency wave model, which is run operationally by the National Weather Service (NWS). The source terms of WW3 include wind input, dissipation, nonlinear interaction, bottom friction, ice scattering, among others.

Since our interest is in  $mss$ , we use the *Ardhuin et al.* [2010] source term package, which is the only reported source term package for WW3 validated for  $mss$ . Along with WW3, this package is open-source to users in most countries. As mentioned earlier, the spectral tail of high-frequency waves is not completely resolved at the time of writing. All third-generation waves thus explicitly model the wave spectrum only up to a certain frequency, and attach a high-frequency tail thereafter. We select a simple  $k^{-3}$  spectral tail, which is suggested by the work of *Banner et al.* [1989], *Forristall* [1981], and *Phillips* [1958]; it was also used recently by *Reichl et al.* [2014] in a high-frequency model based on WW3. The tail is attached at the last frequency modeled by WW3, and thus is completely determined by the value of the spectrum at that frequency. A more elaborate model may include a high-frequency model like that of *Plant* [2015], *Hwang et al.* [2013], or *Elfouhaily* [1997], but this option is not pursued here.

Our WW3 run is driven by the ECMWF operational wind analysis, and has 3 h temporal output resolution and  $0.5^\circ$  latitude and longitude spatial resolution. The last wavenumber before spectral tail attachment is 2.06 rad/m. The  $k^{-3}$  spectral tail ends at  $k_u$ , which is determined by the incidence angle of the track under consideration. For our simulation, the model is driven by wind only; currents play a minimal role globally (*J. Bidlot*, personal communication, 2016)—however, in hurricane conditions, currents can have a significant role [*Fan et al.*, 2009]. We limit ourselves to nonhurricane conditions in this work, and thus neglect currents. In the following, we refer to the WW3 with spectral tail attached as the extended WW3 model.

An example of the attachment of the spectral tail is shown in Figure 3.

## 2.2. GNSS-R Electromagnetic Scattering and Signal Processing Model

The ZV model developed by *Zavorotny and Voronovich* [2000] is a widely used scattering and signal processing model for the GNSS-R received signal. This model is based on geometrical optics (GO) and is valid for a sufficiently rough surface and nongrazing incidence. In practice, the ocean surface can be considered sufficiently rough at wind speeds above about 3 m/s and nongrazing incidence angles are those below

The end-to-end simulator for CYGNSS [*C. S. Ruf et al.*, 2016], which ingests wind speed and generates the delay-Doppler-map, currently uses the Katzberg relationship.

According to the Elfouhaily spectra shown in Figure 2, the long waves contribute a considerable portion of the  $LP_{mss}$  sensitivity to wind. Such characteristics are similar to other spectra [e.g., *Apel*, 1994, Figure 6].

As noted above, the inclusion of a third-generation model, which focuses on the energy-containing long waves, has not been necessary for other sensing techniques. Whether a model would benefit GNSS-R is a question we explore in this work. As third-generation wave models have demonstrated considerable skill in forecasting wave properties near the spectral

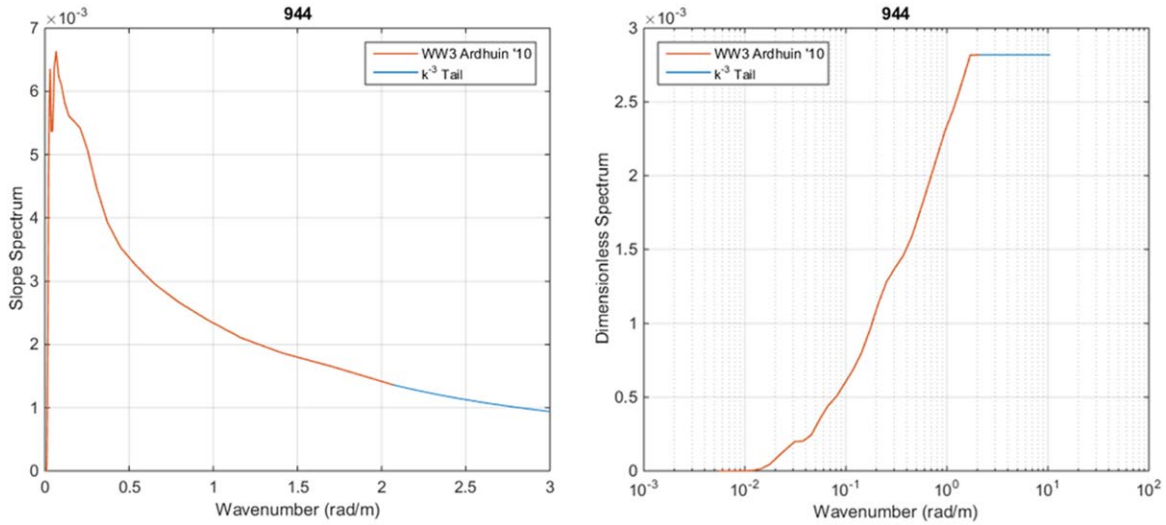


Figure 3. Example of extended WW3 slope spectrum with (a) linear scale (plot upper limit adjusted to 3 rad/m), (b) area conservative form.

about 70°. The received signal is a function of delay and frequency. A two-dimensional plot of the signal power is known as a Delay Doppler Map (DDM) (explained in greater detail in section 3). Because the ZV model connects the wave model and the observables and is pertinent to our signal processing methods, we discuss it here in some detail.

The signal power intercepted by the receiver antenna can be expressed as

$$P_s(\tau, f) = CP_t \iint \frac{G_t G_{rant}}{R_t^2 R_r^2} \chi^2(\Delta\tau, \Delta f) \sigma_0(\vec{s}) dA \tag{5}$$

where  $P_s(\tau, f)$  is the signal power for delay  $\tau$  and frequency  $f$ .  $C$  is a constant that depends on the electromagnetic wavelength and coherent integration period of the receiver.  $P_t$  is the GPS transmitter power and is assumed to be constant, as is  $G_t$ , the product of transmitter antenna and instrument gains.  $G_{rant}$  is the receiver antenna gain and  $R_t, R_r$  are the distances from the dummy integration position on the grid to the transmitter and receiver, respectively. The surface integral is performed over an area large enough for the desired  $\tau$  and  $f$  ranges, and is known as the glistening zone. For us,  $\tau$  ranges over about 30  $\mu$ s and  $f$  ranges over about 10 kHz. The glistening zone is chosen to be 200 km by 200 km centered at the specular point, which is sufficient for most scattering geometries of the TDS-1 instrument considered in section 2.3.

$\Delta\tau = |\tau_g - \tau|$ , with  $\tau_g$  being the delay associated with the location of the differential surface element,  $dA$ .  $\tau_g = (R_t + R_r)/c$  and for a given geometry, it is a constant for a given surface location, independent of  $\tau$  and  $f$ . Similarly,  $\Delta f = f_g - f$ , and  $f_g = -f_{CW}/c(\vec{u}_R \cdot \vec{v}_R + \vec{u}_T \cdot \vec{v}_T)$ .  $f_{CW}$  is the frequency of the carrier wave; for the GPS L1 carrier, it is 1.575 GHz.  $\vec{u}_R$  is the unit vector from the specular point to the receiver,  $\vec{v}_R$  is the receiver velocity vector,  $\vec{u}_T$  is the unit vector from the specular point to the transmitter, and  $\vec{v}_T$  is the transmitter velocity vector.

$\chi^2(\Delta\tau, \Delta f)$  is known as the ambiguity function and models the selectivity of the radar system. Letting  $\tau_0$  and  $f_0$  be the delay and Doppler shift corresponding to the specular point, respectively, if the selectivity is sufficiently high such that  $\frac{G_t G_{rant}}{R_t^2 R_r^2} \sigma_0$  is constant for some small area  $\Delta A$  around the specular point, then, because  $\chi^2(0, 0) = 1$

$$P_{s0} = P_s(\tau_0, f_0) = CP_t \frac{G_t G_{rant}}{R_t^2 R_r^2} \sigma_0 \Delta A \tag{6}$$

We make use of this equation in section 2.3.

Similar to  $\tau_g, f_g, G_t, G_{rant}, R_t,$  and  $R_r, \vec{s}$  is also a constant for a given location (independent of  $\tau, f$ )—it specifies the favorable orientation (two perpendicular slope components) of a facet that reflects the incident ray toward the receiver. The scattering cross section  $\sigma_0(\vec{s})$  is where the surface roughness enters—under

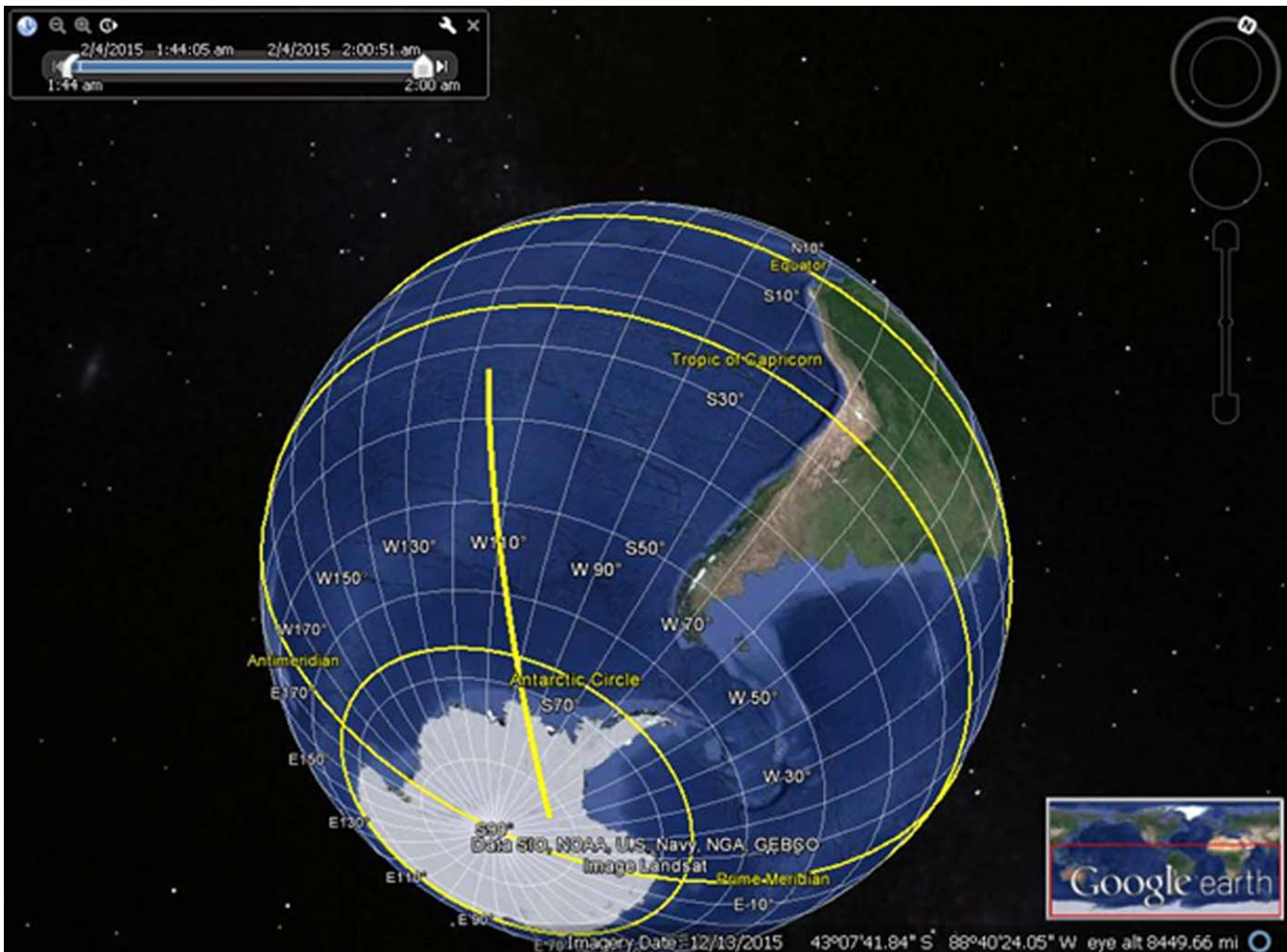


**Figure 4.** The specular point track for RD17 TR407 is shown as the bold yellow line running from Antarctica into the South Pacific. The data are numbered from 1 to 1007, which we call sample number (SN). The transition from land to ocean occurs at SN 264.

geometric optics,  $\sigma_0$  is proportional to the PDF of slopes as well as the square of the Fresnel surface reflectivity. The PDF of slopes and its measurement remain an active area of research [e.g., Cardellach and Rius, 2008; Liu et al., 1997]. To a first order, the PDF of slopes can be approximated by a bivariate Gaussian

$$pdf(s_u, s_c) = \frac{1}{2\pi\sqrt{mss_u mss_c}} \exp\left\{-\frac{1}{2}\left(\frac{s_u^2}{mss_u} + \frac{s_c^2}{mss_c}\right)\right\} \quad (7)$$

where the subscripts u and c denote the upwind and crosswind components. This assumption is also used in Zavorotny and Voronovich [2000]. At the specular point,  $pdf(0, 0)$  is proportional to the inverse of the geometric mean of the mss components. It should be noted that more complex PDFs have also been considered.

In this work, we further assume that the seas are isotropic and the two components of mss are equal. Equivalently, the two-dimensional PDF is rotation-invariant in the sense that it only depends on the magnitude of  $\vec{s}$ . Note that the mss is obtained from WW3 using equation (2).

### 2.3. Model Configuration and Postprocessing for TDS-1

TechDemoSat-1 (TDS-1) is a technology demonstration mission operated by Surrey Satellite Technology Limited (SSTL) [Unwin et al., 2016]. One of its payloads is the Space GNSS Receiver Remote Sensing Instrument (SGR-ReSI), the GNSS-R instrument of interest. TDS-1 has a circular orbit with an altitude of about 630 km. Because there are other instruments on the TDS-1 mission, the SGR-ReSI has limited operating

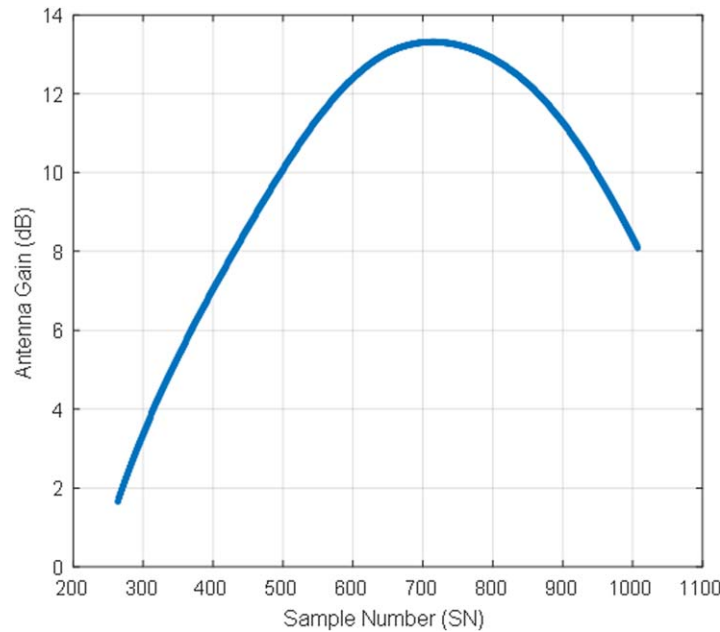


**Figure 5.** Along-track antenna gain for RD17 TR407 for specular points in the ocean; the SN ranges from 264 to 1007.

the ground known as a track. In this work, two surface models are used for computing the mss: the Katzberg model and the extended WW3 model. The GPS transmitter and TDS receiver positions and velocities, along with the TDS receive antenna pattern, are furnished by SSTL. However, the instrument gain is not available; in fact, the receiver has automatic gain control (AGC) turned on, so the instrument gain changes with signal level, and this time-varying gain is not recorded. We therefore process the DDMs in a way that is not sensitive to the gain value, by forming the ratio between their signal and noise regions. The resulting DDMs are of relative received power, normalized by the noise floor of the measurements. They are still sufficiently sensitive to changes in the surface conditions, provided variations in the receiver noise floor are small enough over relevant time scales.

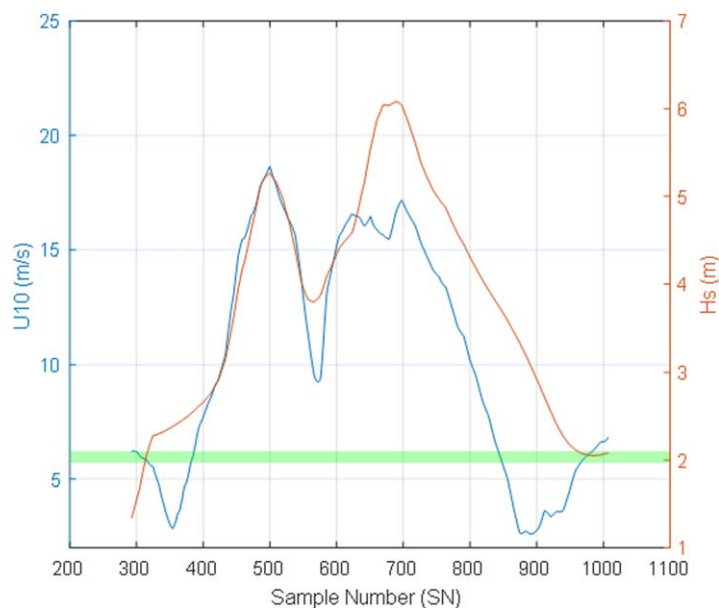


**Figure 6.** (left axis) Along-track U10 and (right axis) Hs. The green band denotes a narrow range of U10 values, the relevance of which is discussed in the text.

time, so the data it collects are limited. In this paper, all references to TDS measurements refer to data collected by the SGR-ReSI.

From section 2.2, several pieces of information are required to compute the received signal. The GPS transmitted power is not published, so it is assumed to be constant. The other parameters needed are:

1. transmitter position and velocity,
2. receiver position and velocity,
3. receiver antenna and instrument (RF and IF) gains, and
4. mss.

All these quantities are functions of time. For a moving receiver, the specular point traces out a trajectory in time across the

The glistening zone is set to 200 km by 200 km. This determines the surface area over which the numerical integration is taken in the model. The wind and mss are assumed to be constant over the area of integration.

In addition to the contribution to the received signal power by scattering from the ocean surface,  $P_s$  in equation (5) also contains other components due to radiometric thermal emission by the scene, noise due to the receiver instrumentation (including the antenna), and radio-frequency interference (RFI) [e.g., *Chen and Ruf, 2015*]. We neglect RFI in this paper. The total received signal (in uncalibrated

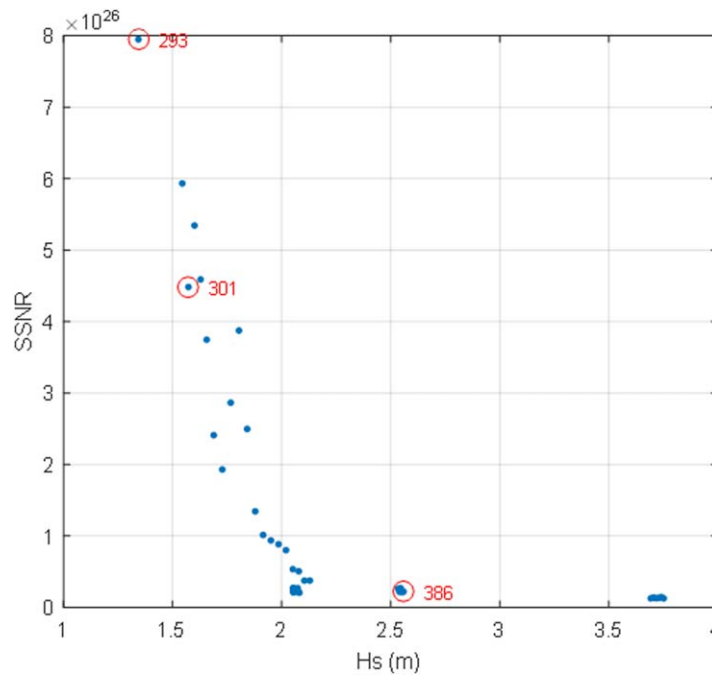


**Figure 7.** Measurement SSNR observable versus Hs with U10 between 5.7 and 6.2 m/s—this range is shown by the green band in Figure 6.

units of counts) can then be modeled as

$$C_T(\tau, f) = G_{ri}(P_N + P_s) \quad (8)$$

where  $G_{ri}$  is the receiver instrument gain (excluding the antenna gain) and  $P_N$  is the total noise power.  $P_N$  includes the radiometric thermal emission from the scene referred to the output of the antenna and the noise due to receiver instrumentation.  $P_s$  is the GNSS-R signal power, given by the ZV model in equation (5). To be precise,  $P_s$  is the ensemble mean of the signal power. In practice, there will also be speckle noise present in the measurements. Our model neglects the speckle noise and estimates the ensemble mean.

The noise contributions to the measurements are estimated by examining pixels of the

DDM at delay values that correspond to altitudes higher than the surface. As such, these pixels contain no scattered surface signal and  $P_s = 0$  can be assumed. In that case, the uncalibrated measurements can be written as

$$C_N = G_{ri}(P_N) \quad (9)$$

The pixel in the DDM with the highest power is assumed to correspond to the specular point location. This is only approximate, as the peak power originates from a region near but not necessarily at the specular point. With two equations  $C_T(\tau_0, f_0) = G_{ri}(P_N + P_s(\tau_0, f_0))$  and  $C_N = G_{ri}(P_N)$ , we cannot completely resolve the three unknowns,  $P_s(\tau_0, f_0)$ ,  $G_{ri}$ , and  $P_N$ . It should be noted that the upcoming CYGNSS mission carries an augmented version of the receiver that incorporates calibration targets and fixed receiver gain, so these unknowns can be determined. For TDS, no absolute calibration can be performed and the DDMA observable [Clarizia et al., 2014] is not easily computed. (An observable is a single number characterization of the DDM.)

Because of this, a proxy for the DDMA, known as the SNR [Jales, 2015], is now being used in the TDS community. It is defined by

$$SNR = \frac{C_T(\tau_0, f_0) - C_N}{C_N} = \frac{G_{ri}(P_N + P_s) - G_{ri}(P_N)}{G_{ri}(P_N)} = \frac{G_{ri}(P_s)}{G_{ri}(P_N)} = \frac{P_s}{P_N} \quad (10)$$

We see that the SNR observable is independent of gain as desired, but depends on the noise power. Gain varies much faster than the noise power—the dominant factor is changes due to instrument temperature and AGC adjustments.

For our simulations, we only model  $P_s$  and do not model the thermal noise. To estimate  $P_N$ , we compute the ratio between the measured SNR and the modeled  $P_s$  over an entire track. Thus:

$$P_N = \frac{E[P_s^{sim}]}{E[SNR^{TDS}]} \quad (11)$$

where  $E[\cdot]$  is the time average operator,  $P_s^{sim}$  is the simulated signal power, and  $SNR^{TDS}$  is the TDS-measured SNR. This assumes that  $P_N$  is constant over the track, and there are no biases to  $P_s$ . With  $P_N$  known, the simulated SNR can then be computed.



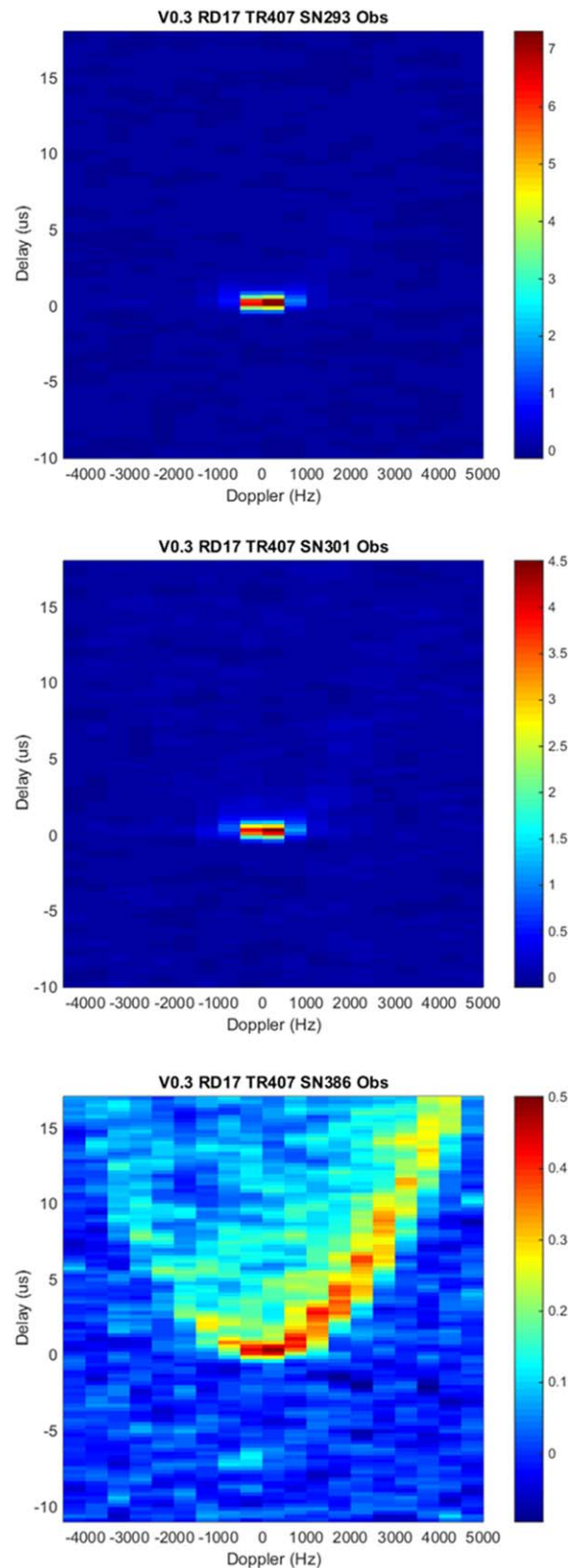


**Figure 8.** TDS Measurements. (top) SN 293 with  $H_s = 1.34$  m and  $U_{10} = 6.19$  m/s. (middle) SN 301 with  $H_s = 1.57$  m and  $U_{10} = 6.18$  m/s. (bottom) SN 386 with  $H_s = 2.13$  m and  $U_{10} = 5.70$  m/s.

The computation of modeled SNR requires the extraction of a single parameter from the measurements. Note that there are other observables that could alternately be used, such as the DDM volume observable [Marchan-Hernandez et al, 2008]. This observable, fundamentally, makes use of the ratio of the signal powers from DDM bins far away from the specular point to those at or near the specular point. We have considered this observable in our analysis and the results are similar in character to those using the SNR presented in section 3, but they are found to exhibit a large noise level than the SNR observable. For this reason, we will use an SNR-related observable in the following discussions.

To focus on the effects of sea state, we define the Scaled SNR as:

$$SSNR = SNR \frac{R_{tSP}^2 R_{rSP}^2}{G_{rant}} \quad (12)$$

where  $R_{tSP}$  and  $R_{rSP}$  are the distances from the specular point to the transmitter and receiver, respectively.

We neglect scaling corrections for scattering area and incidence angle-dependent Fresnel reflectivity for simplicity and because the measurement geometries present in the TDS sample population do not exhibit significant variations.

Last, we note that for a given geometry, higher mss values (greater roughness) correspond to smaller SNR values.

### 3. Results and Discussion

We analyze one TDS track in this work: Track 407 in RD 17 of SSTL’s Version 0.3 data set. This track contains about 16 min of continuous data, collected by a single receiver channel and a single GPS transmitter (GPS PRN #10 and Receiver Channel #2, per SSTL’s numbering conventions). One DDM is produced every second. This track exhibits a good variation of coastal and oceanic conditions, as well as a variety of sea states. The track of the specular point is plotted in Figure 4.

The receive antenna gain along the track is plotted in Figure 5. The variation in gain results from the progression of transmitter and receiver locations, and the resulting change in measurement geometry, over time.

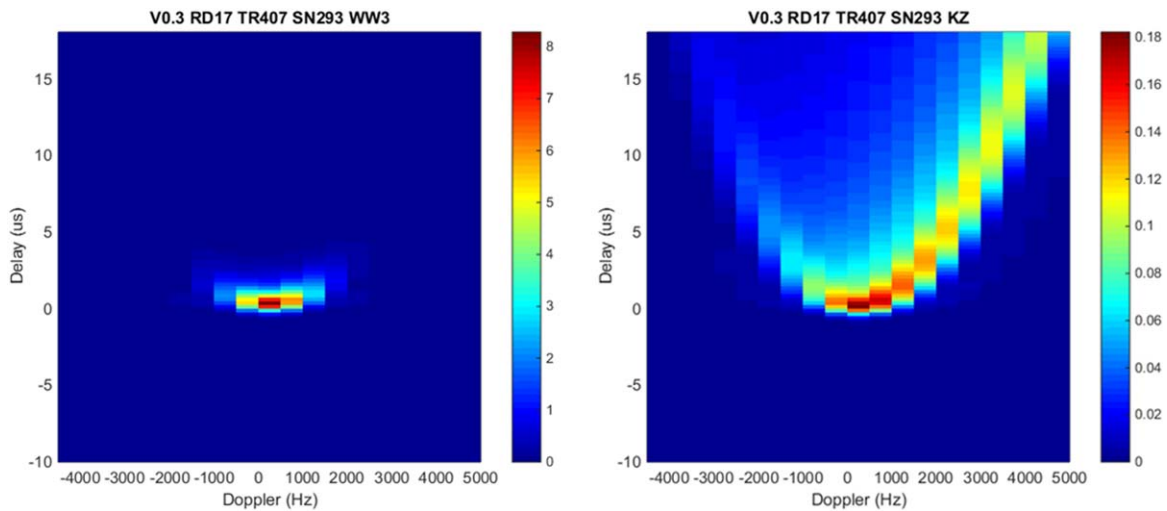


**Figure 9.** DDMs predicted by the two forward models: (left) WW3 and (right) Katzberg given ocean conditions  $H_s = 1.34$  m and  $U_{10} = 6.19$  m/s consistent with observation SN 293. Compare to the top plot in Figure 8. For WW3, the DDM is in good agreement with the observation. For Katzberg, both the shape and signal magnitude show large discrepancies.

Because antenna gain can affect the signal quality, we consider only measurements with gain greater than 3 dB in our analysis. In addition, since our interest is in ocean GNSS-R, we filter out any data with its specular point located less than 100 km away from the coast. The resulting data set has sample numbers ranging from 293 to 1007. This is the rationale for restricting the grid size to be 200 km by 200 km as mentioned in section 2. Relative to the specular point, delay, and Doppler bins with less than  $18 \mu\text{s}$  and 5000 Hz in either direction are considered, and this is the range plotted in the DDMs shown below. The average incidence angle for the track under consideration is  $13.8^\circ$ , which results in a cut-off wavenumber,  $k_w$ , of 10.59 rad/m or 59 cm in wavelength.

### 3.1. Empirical Evidence of Measurement Sensitivity to Significant Wave Height

As seen from equations (2) and (3), significant wave height,  $H_s$ , is much more sensitive to long waves than the mean square slope. These long waves include swell that is not correlated with wind. In this subsection, we explore the dependence of SSNR (and thus mss) on  $H_s$  using TDS measurements.

In Figure 6,  $U_{10}$  and  $H_s$  are plotted against sample number (SN) for Track 407. Each SN is separated by approximately one second, and, for this track, the specular points of two consecutive measurements are spaced about

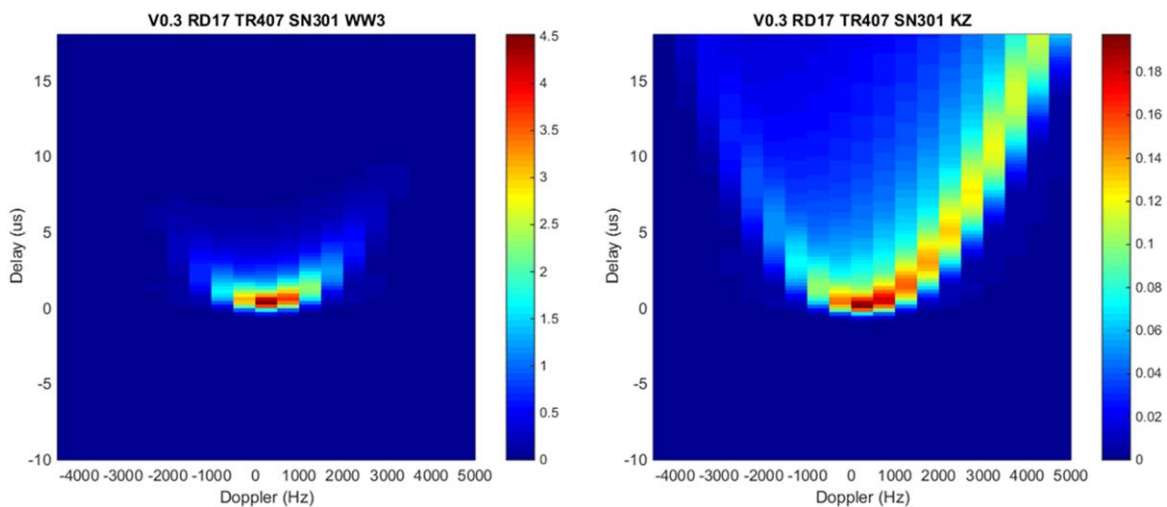


**Figure 10.** DDMs predicted by the two forward models: (left) WW3 and (right) Katzberg given ocean conditions  $H_s = 1.57$  m and  $U_{10} = 6.18$  m/s consistent with observation SN 301. Compare to the middle plot in Figure 8. For WW3, the DDM is in good agreement with the observation. For Katzberg, both the shape and signal magnitude show large discrepancies.

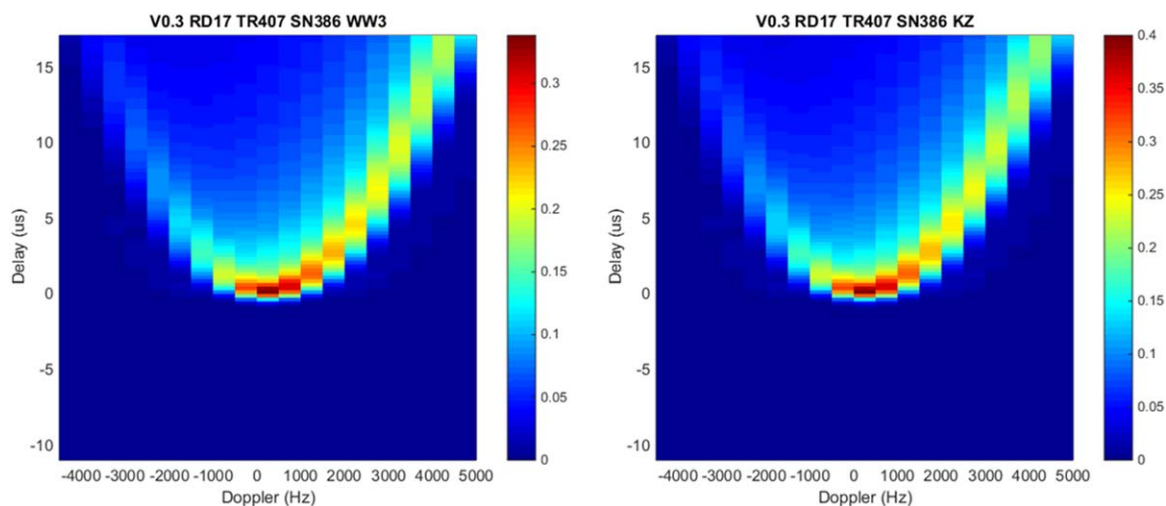


**Figure 11.** DDMs predicted by the two forward models: (left) WW3 and (right) Katzberg given ocean conditions  $H_s = 2.13$  m and  $U_{10} = 5.70$  m/s consistent with observation SN 386. Compare to the bottom plot in Figure 8. Both models are both in good agreement with the observations.

6000 m apart.  $H_s$  is obtained from spatial interpolation of the same WW3 model run, as WW3 is skillful in modeling  $H_s$ .  $U_{10}$  comes from the same ECMWF wind reanalysis product that is used to force the WW3 model.

Although  $U_{10}$  exhibits some correlation with  $H_s$ , there are many points where they deviate from one another. To control for  $U_{10}$  and examine the variance of the SSNR explained by  $H_s$  alone, we restrict our analysis to measurements for which  $U_{10}$  lies in the narrow range between 5.7 and 6.2 m/s. This region is shaded by a horizontal green band in Figure 6. A scatterplot of the measured SSNR versus  $H_s$  values in this region is shown in Figure 7.

$H_s$  is seen to have a strong effect on SSNR that cannot be accounted for solely by wind speed. This behavior has been noted previously [Soisuvann *et al.*, 2016]. Some scatter is also seen, indicating that SSNR has additional variability explained by neither  $H_s$  nor wind speed. In the figure, we have picked three representative measurements; these are circled in red with their SNs indicated. We examine their DDMs in this and the next subsections.

The three DDMs measured by TDS are presented in Figure 8. Both the magnitude and shape of the DDMs change significantly. The magnitude decreases monotonically as  $H_s$  increases, which is consistent with theoretical expectations. The  $m_{ss}$  corresponding to each of the DDMs can be estimated using either the Katzberg or WW3 model. In the case of Katzberg, all three wind speeds are nearly the same, so the  $m_{ss}$  is, too. It is 0.0172. With the WW3 model,  $m_{ss}$  is not solely dependent on wind speed and the  $m_{ss}$  is found to be 0.00028, 0.00063, and 0.0122 for SN 293, 301, and 386, respectively. The significant differences in  $m_{ss}$  with the WW3 model are due to other influences on the local sea state than simply the wind speed there. In particular, note that the significant wave height varies significantly between the three cases.

### 3.2. Modeling the Effect of Significant Wave Height on the Measurement

In this subsection, we examine modeled results and compare them to the measurements in the previous subsection. First, we look at the modeled DDMs of the three cases considered. Second, we look at the dependence on  $H_s$  predicted by the models. Last, we look at the along-track plots of the SSNR.

Because the windspeed is essentially the same in all three cases, the Katzberg DDMs should all look about the same. This is indeed the case, as seen the modeled DDMs in Figures 9–11 (right plots). The left plots show the results of the extended WW3 model. Comparing to the TDS measurements in Figure 8, it is seen that the WW3-based model is much better able to represent the behavior of the measurements, compared to the Katzberg model, in both the magnitude and shape of the DDMs.

We now plot modeled SSNR versus  $H_s$  in Figure 12. These plots reaffirm WW3's skill over the Katzberg model. In particular, significant improvement is seen for low  $H_s$  values; these were found to

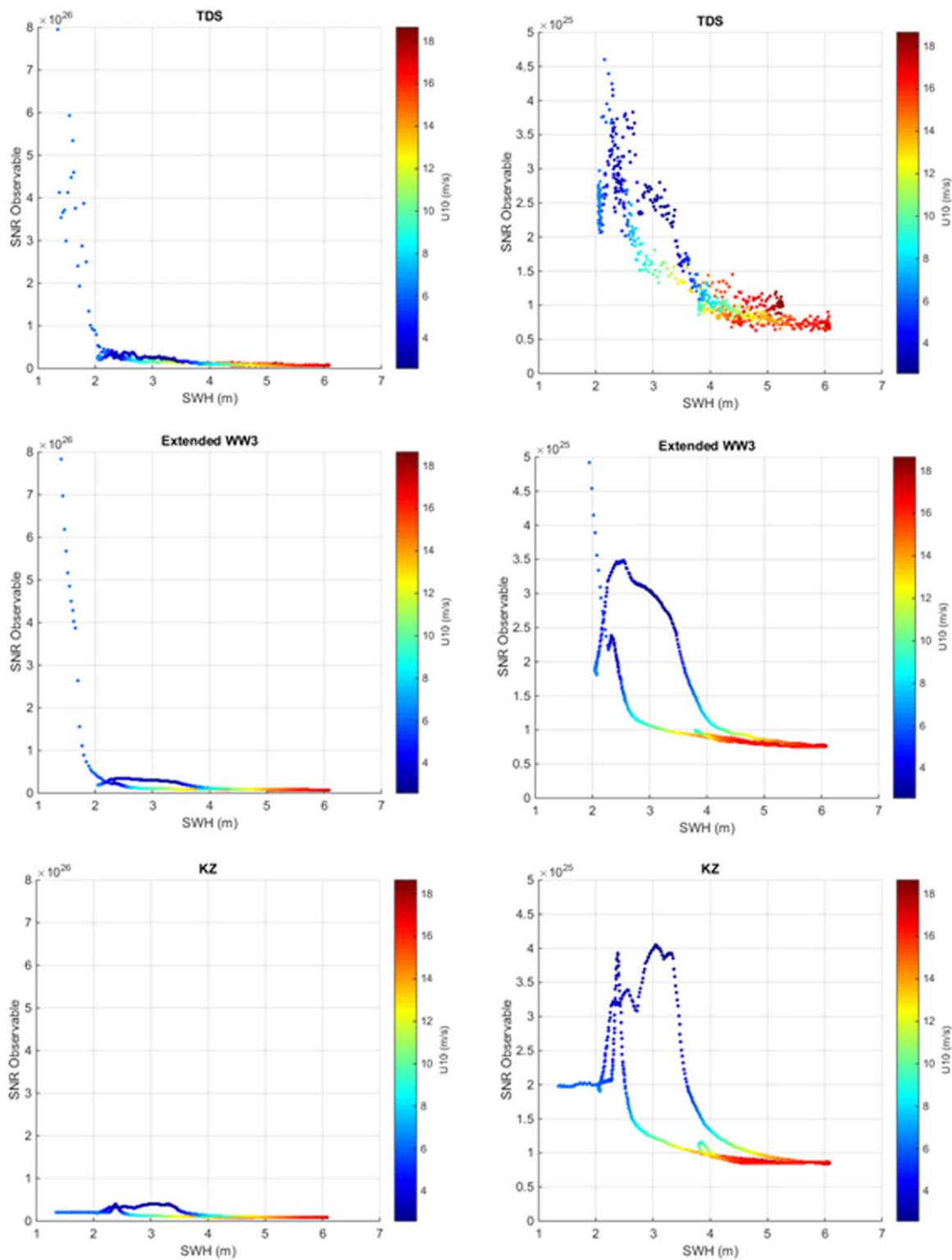


**Figure 12.** SSNR versus SWH, with U10 color-coded. The figures in the right column are zoomed in versions of the ones on the left. (a) TDS—these two plots are characteristically the same as Figure 7, but no filtering is done based on U10 (b) extended WW3, (c) Katzberg. Because of the inverse dependence of mss, SNR is much more sensitive to mss changes when mss is small.

occur at the beginning of the track near the coast. In addition, the Katzberg model demonstrates deficiencies in the “branch” near  $H_s = 3$  m and  $SSNR = 3e25$ ; these correspond to very low wind-speeds of less than 3 m/s.

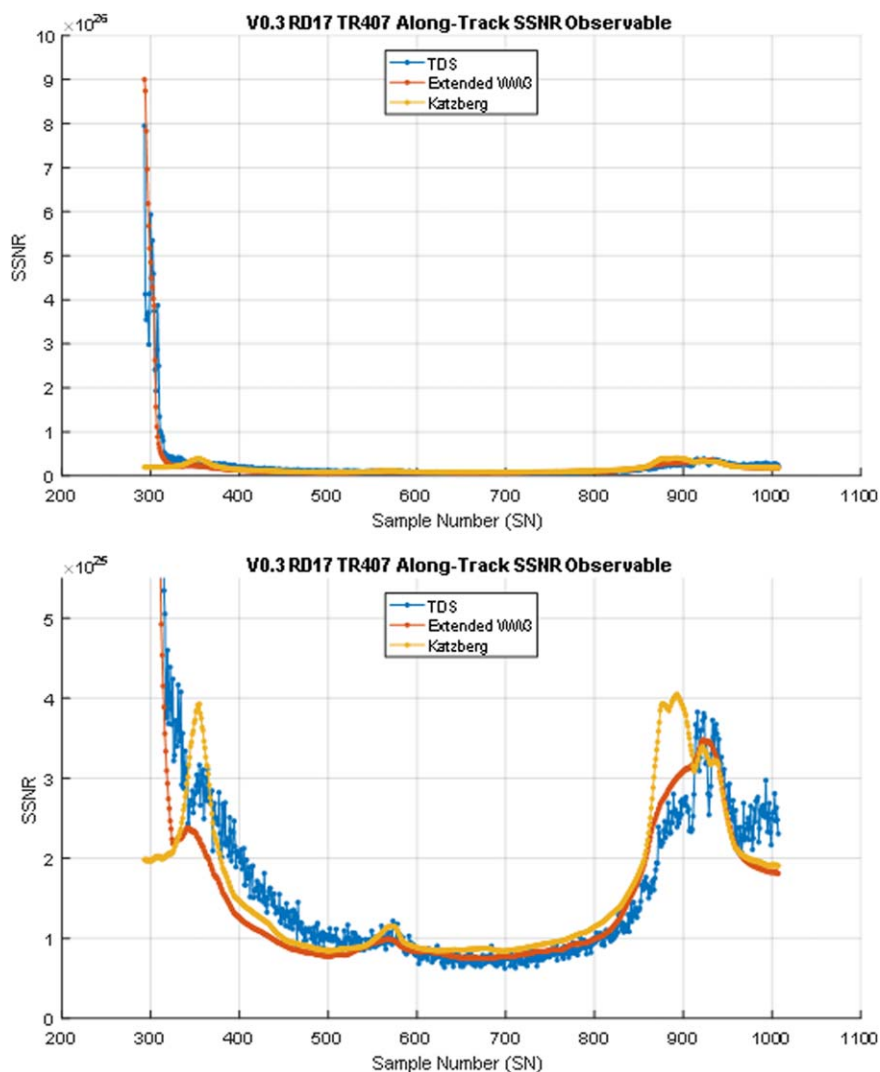


**Figure 13.** (a) Along-track plot of measured SSNR, extended WW3 SSNR, Katzberg SSNR, and scaled  $H_s$  and  $U_{10}$ . (b) Zoomed in version of Figure 13a.

To gain additional insight, we plot the SSNR versus along-track SN for the TDS measurements and both models in Figure 13. This figure should be used in conjunction with Figure 6, which shows the along-track  $U_{10}$  and  $H_s$ . Using the variance of the difference between simulations and measurements as the metric, the extended WW3 model shows a 68.7% improvement over the Katzberg model over the entire track. The improvements in the coastal region at the start of the track is one significant contributor. If we consider only SN 342 and higher, we still see a 30.2% improvement in the skill of the extended WW3 model. This improvement can largely be attributed to the SNs 850–900, for which the wind speed is very low.

Another insight is that despite the attachment of a diagnostic tail, we see WW3 is also responsive to local wind: at SNs from about 900–950,  $H_s$  is decreasing but wind speed is increasing (see Figure 6). WW3 is able to model the decreasing behavior of the observable correctly.

This analysis shows that the extended WW3 model has considerable skill modeling the GNSS-R observable, derived from its ability to take nonlocal long waves into account, and in modeling the sea state in low-wind speed conditions.

One implication of our results is that much of the sensitivity of the GNSS-R observable to the sea state derives from long and intermediate-scale waves of wavenumber 2 rad/m and lower. This is consistent with

predictions of the parametric Elfouhaily model shown in Figure 2. However, it should be noted that this track does not contain winds that change quickly in time. A track with rapid changes in wind temporally and spatially will be able to better evaluate whether the diagnostic tail should be replaced one that has an explicit wind speed dependence. Fast changes in wind may also necessitate that the model be run at a higher spatial and temporal resolution with the corresponding wind speed products.

Last, we note that both models show overly low SSNRs between serial numbers 350 and 500, while a slightly positive bias is seen between 600 and 850. These discrepancies can be the result of an overall, constant bias that is not removed before determining and applying the SSNR scale factor in equation (11). Such a bias may be due to errors in the cutoff  $k_{ur}$ , or the spectral level. This bias may also contribute to the difference in shapes of the measured and WW3 DDMs shown in Figures 8 and 10.

#### 4. Conclusions and Future Work

In this work, we have developed a GNSS-R forward model that incorporates a third-generation surface wave model. The analysis of one track of TDS measurements, with over 700 consecutive DDMs, shows that this model can account for observable dependencies on the local wind as well as other, non-local effects. In contrast to conventional remote sensing techniques, the nonlocal effects are significant for GNSS-R due to frequency and geometry. The model demonstrates improved skill over the widely used Katzberg one-to-one wind speed-mss model. Significant improvements are seen in low-wind conditions, in particular. The novelty and strength of the model is derived from the WW3 model, the source terms of which are the result of decades of work by the wave modeling, experimental, and remote sensing communities. Conversely, given the demonstrated sensitivity of GNSS-R to ocean surface wave spectra, the assimilation of its measurements into numerical wave models may also provide valuable constraints on the derived sea state.

The use of a third generation wave model in GNSS-R forward modeling has great potential for future work. Some ideas include:

1. retrieval of mss from the measurements, and taking into account scattering area and Fresnel reflectivity,
2. modeling of anisotropic seas with two mss components and a more sophisticated pdf of slopes, in effect creating a tighter coupling between the scattering and wave models,
3. relaxation of assumption of uniformity of wind and mss fields over the 200 km by 200 km glistening zone,
4. augmenting the scattering model by taking the coherent scattering component into account for low-wind speeds,
5. usage of CYGNSS data when it becomes available; with absolute calibration, better signal quality can be achieved, and
6. addition of wave-current interactions in the wave model.

To understand the underlying physical phenomena modeled by WW3 that allows it to produce better long-wave mss, it would be helpful to examine the two-dimensional wave spectra, as well as the source term spectra. Those insights may lead to the development of ancillary parameters that could be helpful in constructing better wind retrieval algorithms for GNSS-R.

The model presented here can also be used to improve our understanding of surface waves with GNSS-R measurements. Possibilities include the tuning of the spectral tail and development of appropriate source terms. The model is also expected to be helpful in the design of future GNSS-R missions and experiments.

#### Acknowledgments

This work was funded in part by the National Aeronautics and Space Administration (grant NNX13AP93H and contract NNL13AQ00C). TechDemoSat-1 data used in this study are available from the publically accessible MERRByS web site at <http://www.merrbys.co.uk>. Wavewatch III data used in this study are available from the publically accessible NOAA web site at <http://polar.ncep.noaa.gov/waves/ensemble/download.shtml>.

#### References

- Apel, J. R. (1994), An improved model of the ocean surface wave vector spectrum and its effects on radar backscatter, *J. Geophys. Res.*, 99(C8), 16,269–16,291, doi:10.1029/94JC00846.
- Arduin, F. (2016), *Ocean Waves in Geosciences*, Université de Bretagne Occidentale, France. [Available at [ftp://ftp.ifremer.fr/ifremer/ww3/COURS/waves\\_in\\_geosciences\\_2016.pdf](ftp://ftp.ifremer.fr/ifremer/ww3/COURS/waves_in_geosciences_2016.pdf), accessed: 29 Jul, 2016.]
- Arduin, F., et al. (2010), Semiempirical dissipation source functions for ocean waves. Part I: Definition, calibration, and validation, *J. Phys. Oceanogr.*, 40, 1917–1941, doi:10.1175/2010JPO4324.1.

- Banner, M. L., I. S. F. Jones, and J. C. Trinder (1989), Wavenumber spectra of short-gravity waves, *J. Fluid Mech.*, *198*, 321–344, doi:10.1017/S0022112089000157.
- Booij, N., R. C. Ris, and L. H. Holthuijsen (1999), A third-generation wave model for coastal regions, Part I, Model description and validation, *J. Geophys. Res.*, *104*(C4), 7649–7666.
- Brown, G. (1978), Backscattering from a Gaussian distributed perfectly conducting rough surface, *IEEE Trans. Antennas Propag.*, *AP-26*(3), 472–482.
- Cardellach, E., and A. Rius (2008), A new technique to sense non-Gaussian features of the sea surface from L-band bi-static GNSS reflections, *Remote Sens. Environ.*, *112*(6), 2927–2937, doi:10.1016/j.rse.2008.02.003.
- Cardellach, E., S. G. Jin, and F. Xie (2014), *Chapter 9 of GNSS Remote Sensing: Theory, Methods and Applications*, Springer, New York, London.
- Chen, D. D. and C. S. Ruf (2015), Adaptive control of undetected radio frequency interference with a space borne microwave radiometer, *IEEE Trans. Geosci. Remote Sens.*, *53*(9), 4972–4984, doi:10.1109/TGRS.2015.2414395.
- Chen, D. D., C. S. Ruf, and S. T. Gleason (2016), Response time of mean square slope to wind forcing: An empirical investigation, *J. Geophys. Res. Oceans*, *121*, 2809–2823, doi:10.1002/2016JC011661.
- Chu, P. C., Y. Qi, Y. Chen, P. Shi, and Q. Mao (2004), South China Sea wind-wave characteristics. Part I: Validation of wavewatch-III using TOPEX/Poseidon data, *J. Atmos. Oceanic Technol.*, *21*, 1718–1733, doi:10.1175/JTECH1661.1.
- Clarizia, M. P., C. Ruf, P. Jales, and C. Gommenginger (2014), Spaceborne GNSS-R minimum variance wind speed estimator, *IEEE Trans. Geosci. Remote Sens.*, *52*(11), 6829–6843, doi:10.1109/TGRS.2014.2303831.
- Donelan, M. A., M. Curcic, S. S. Chen, and A. K. Magnusson (2012), Modeling waves and wind stress, *J. Geophys. Res.*, *117*, C00J23, doi:10.1029/2011JC007787.
- Elfouhaily, T., B. Chapron, K. Katsaros, and D. Vandemark (1997), A unified directional spectrum for long and short wind-driven waves, *J. Geophys. Res.*, *102*(C7), 15,781–15,796.
- Fan, Y., I. Ginis, and T. Hara (2009), The effect of wind–wave–current interaction on air–sea momentum fluxes and ocean response in tropical cyclones, *J. Phys. Oceanogr.*, *39*, 1019–1034, doi:10.1175/2008JPO4066.1.
- Forristall, G. Z. (1981), Measurements of a saturated range in ocean wave spectra, *J. Geophys. Res.*, *86*(C9), 8075–8084, doi:10.1029/JC086iC09p08075.
- Fu, L.-L., E. J. Christensen, C. A. Yamarone, Jr., M. Lefebvre, Y. Ménard, M. Dorrer, and P. Escudier (1994), TOPEX/POSEIDON mission overview, *J. Geophys. Res.*, *99*(C12), 24,369–24,381, doi:10.1029/94JC01761.
- Gleason, S., C. Ruf, M. P. Clarizia, A. O'Brien (2016), Calibration and unwrapping of the normalized scattering cross section for the Cyclone Global Navigation Satellite System (CYGNSS), *IEEE Trans. Geosci. Remote Sens.*, *54*(5), 2495–2509, doi:10.1109/TGRS.2015.2502245.
- Hasselmann, K. et al. (1973), Measurements of wind-wave growth and swell decay during the Joint North Sea Wave Project (JONSWAP), *Dtsch. Hydrog. Z., Suppl. A*, *8*(12), 95.
- Hwang, P. A. (2005), Wave number spectrum and mean square slope of intermediate-scale ocean surface waves, *J. Geophys. Res.*, *110*, C10029, doi:10.1029/2005JC003002.
- Hwang, P. A., and F. Fois (2015), Surface roughness and breaking wave properties retrieved from polarimetric microwave radar backscattering, *J. Geophys. Res. Oceans*, *120*, 3640–3657, doi:10.1002/2015JC010782.
- Hwang, P. A., and D. W. Wang (2004), Field measurements of duration-limited growth of wind-generated ocean surface waves at young stage of development, *J. Phys. Oceanogr.*, *34*, 2316–2326, doi:10.1175/1520-0485(2004)034<2316:FMODGO>2.0.CO;2.
- Hwang, P. A., D. M. Burrage, D. W. Wang, and J. C. Wesson (2013), Ocean surface roughness spectrum in high wind condition for microwave backscatter and emission computations, *J. Atmos. Oceanic Technol.*, *30*, 2168–2188, doi:10.1175/JTECH-D-12-00239.1.
- Jales, P. (2015), *MERRByS Product Manual: GNSS Reflectometry on TDS-1 with the SGR-ReSI, Tech. Rep. SSTL Rep. 0248366*, revision 001, Surrey Satellite Technol. Ltd., Guildford, U. K. [Available at <http://www.merrbys.co.uk>]
- Katzberg, S. J., J. Dunion, and G. G. Ganoe (2013), The use of reflected GPS signals to retrieve ocean surface wind speeds in tropical cyclones, *Radio Sci.*, *48*, 371–387, doi:10.1002/rds.20042.
- Komen, G. J., L. Cavaleri, M. Donelan, K. Hasselmann, S. Hasselmann, and P. A. E. M. Janssen, (Eds.) (1994), *Dynamic and Modelling of Ocean Waves*, 532 pp., Cambridge Univ. Press, Cambridge, U. K.
- Lin, B., S. J. Katzberg, J. L. Garrison, and B. A. Wielicki (1999), Relationship between GPS signals reflected from sea surfaces and surface winds: Modeling results and comparisons with aircraft measurements, *J. Geophys. Res.*, *104*(C9), 20,713–20,727, doi:10.1029/1999JC900176.
- Liu, Y., X. H. Yan, W. T. Liu, and P. A. Hwang (1997), The probability density function of ocean surface slopes and its effects on radar backscatter, *J. Phys. Oceanogr.*, *27*(5), 782–797.
- Lyzenga, D. R., and J. R. Bennett (1988), Full-spectrum modeling of synthetic aperture radar internal wave signatures, *J. Geophys. Res.*, *93*(C10), 12,345–12,354, doi:10.1029/JC093iC10p12345.
- Marchan-Hernandez, J. F., N. Rodriguez-Alvarez, A. Camps, X. Bosch-Lluis, I. Ramos-Perez, and E. Valencia (2008), Correction of the sea state impact in the L-band brightness temperature by means of delay-Doppler maps of global navigation satellite signals reflected over the sea surface, *IEEE Trans. Geosci. Remote Sens.*, *46*(10), 2914–2923, doi:10.1109/TGRS.2008.922144.
- Pierson W. J., and L. Moskowitz (1964), A proposed spectral form for fully developed wind seas based on the similarity theory of S.A. Kitai-gordskii, *J. Geophys. Res.*, *69*(24), 5181–5190.
- Phillips, O. M. (1958), The equilibrium range in the spectrum of wind generated waves, *J. Fluid Mech.*, *4*, 426–434.
- Plant, W. J. (2015), Short wind waves on the ocean: Wavenumber-frequency spectra, *J. Geophys. Res. Oceans*, *120*, 2147–2158, doi:10.1002/2014JC010586.
- Reichl, B. G., T. Hara, and I. Ginis (2014), Sea state dependence of the wind stress over the ocean under hurricane winds, *J. Geophys. Res. Oceans*, *119*, 30–51, doi:10.1002/2013JC009289.
- Ruf, C., et al. (2016), *CYGNSS Handbook*, 154 pp, Michigan Publ., Ann Arbor.
- Ruf, C. S., et al. (2016), New Ocean winds satellite mission to probe hurricanes and tropical convection, *Bull. Am. Meteorol. Soc.*, 385–395, doi:10.1175/BAMS-D-14-00218.1.
- Soisuvarn, S., Z. Jelenak, F. Said, P. S. Chang, and A. Egido (2016), The GNSS reflectometry response to the ocean surface winds and waves, *IEEE J. Sel. Topics Appl. Earth Observ. Remote Sens.*, *9*(10).
- The Wamdi Group (1988), The WAM model: A third generation ocean wave prediction model, *J. Phys. Oceanogr.*, *18*, 1775–1810, doi:10.1175/1520-0485(1988)018<1775:TWMTGO>2.0.CO;2.
- Tolman, H. L., and the WAVEWATCH III Development Group (2014), User Manual and System Documentation of WAVEWATCH III, version 4.18, *NOAA/NWS/NCEP/MMAB Tech. Note*, 316, National Oceanographic and Atmospheric Administration, U.S. Government.

- Unwin, M., P. Jales, J. Tye, C. Gommenginger, G. Fotti, and J. Rosello (2016), Spaceborne GNSS-reflectometry on TechDemoSat-1: Early mission operations and exploitation, *IEEE J. Sel. Topics Appl. Earth Observ. Remote Sens.*, *9*(10), doi:10.1109/JSTARS.2016.2603846.
- Valenzuela, G. R. (1978), Theories for the interaction of electromagnetic and oceanic waves: A review, *Boundary Layer Meteorol.*, *13*, 61.
- Voronovich, A. G., and V. U. Zavorotny (2001), Theoretical model for scattering of radar signals in Ku and C bands from a rough sea surface with breaking waves, *Waves Rand. Media*, *11*, 247–269.
- Zavorotny, V. U., and A. G. Voronovich (2000), Scattering of GPS signals from the ocean with wind remote sensing application, *IEEE Trans. Geosci. Remote Sens.*, *38*(2), 951–964, doi:10.1109/36.841977.
- Zavorotny, V. U., S. Gleason, E. Cardellach, and A. Camps (2014), Tutorial on remote sensing using GNSS bistatic radar of opportunity, *IEEE Geosci. Remote Sens. Mag.*, *2*(4), 8–45, doi:10.1109/MGRS.2014.2374220.